# Electro-osmotic instability and chaos: membranes, polarizable surfaces, and cross-flow

**By M. B. Andersen, C. L. Druzgalski, S. M. Davidson, J. W. Nichols AND A. Mani**

## 1. Motivation and objectives

Despite century-old developments in the fields of electrokinetics and electrochemistry, the fundamental phenomenon of ionic transport above the diffusion-limited current across a charge-selective surface in aqueous electrolytes is still not fully understood (Nikonenko *et al.* 2010). Charge-selective surfaces include ion-selective membranes (Druzgalski *et al.* 2013), electrodes (Newman & Thomas-Alyea 2004), and nanochannels (Zangle *et al.* 2010), and are used in applications such as electrodialysis/desalination (Strathmann 2010), flow batteries (Weber *et al.* 2011), electrodeposition (Newman & Thomas-Alyea 2004), lab-on-a-chip bioanalysis (Wang *et al.* 2005), fuel cells, and the production of chemicals (Pourcelly *et al.* 2012).

Levich recognized that the transport at large voltages becomes rate-limited by diffusion from a well-stirred bulk to an ion-depleted charge-selective surface (see Figure 1a) (Levich & Spalding 1962). For currents above the diffusion-limit, several theories for possible mechanisms have been proposed including electro-osmotic instability (EOI) (Rubinstein & Zaltzman 2000; Zaltzman & Rubinstein 2007), water splitting (Simons 1979), and current-induced membrane discharge (Andersen *et al.* 2012). Accumulating experimental evidence has made it clear that EOI mixes the diffusion layer and enhances the transport in the overlimiting regime (Maletzki *et al.* 1992; Chang *et al.* 2012).

EOI develops due to electrostatic body forces in a charged boundary layer, the so-called extended space charge (ESC), that forms when voltages larger than a few times the thermal voltage $O(25\text{ mV})$ are applied across the system. The ESC is one of several electrochemical boundary layers and it emerges between the electric double layer (EDL) and the diffusion layer (DL). For a more thorough exposition of EOI, we refer the reader to our recent publication (Druzgalski *et al.* 2013).

In this brief, after introducing the governing equations in Section 2, we explain our recent research on EOI in three different settings. In Section 3, we study overlimiting transport in a well-stirred stationary reservoir at a flat ion-selective surface (see Figure 1a). This study demonstrates for the first time that EOI transitions into fully chaotic flow. In Section 4, we extend our first analysis by considering the transport at a cylindrical and inert metallic electrode (see Figure 4) and show for the first time the development of EOI and chaotic flow in this type of system. In Section 5, we do a linear stability analysis of an electrodialysis system where we account for the cross-flow (see Figure 1b) and show that it has a stabilizing effect on the EOI.

## 2. Governing equations

Our starting point is the incompressible Navier–Stokes equations Eq. (2.1a,b) and Poisson–Nernst–Planck equations Eq. (2.1c,d) for a symmetric binary electrolyte in the

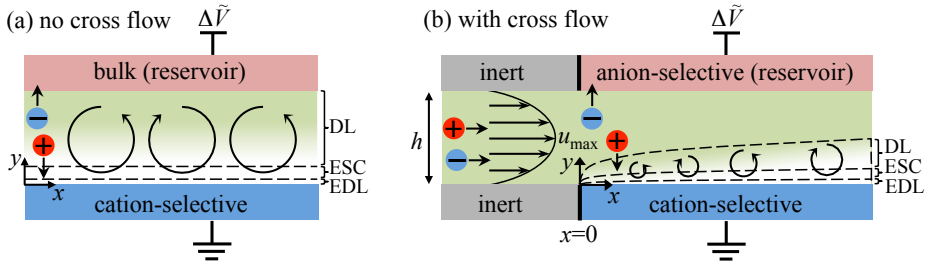


FIGURE 1. Sketch of electroosmotic instability of concentration polarization between parallel plates (a) without cross-flow and (b) with cross-flow. Indicated are the electric double layer (EDL), the extended space charge (ESC) layer, and the diffusion layer (DL). In this work the anion-selective plate is idealized as a reservoir, to allow focus on only a single unstable boundary layer.

dilute limit. Here we present these governing equations where the dimensional quatities are denoted by asterisks,

$$\rho^*\left[\frac{\partial \boldsymbol{v}^*}{\partial t^*}+\left(\boldsymbol{v}^*\cdot\boldsymbol{\nabla}^*\right)\boldsymbol{v}^*\right]=-\boldsymbol{\nabla}^* p^*+\mu^*\nabla^{*2}\boldsymbol{v}^*+\rho_e^*\boldsymbol{E}^*, \tag{2.1a}$$

$$\boldsymbol{\nabla}^*\cdot\boldsymbol{v}^*=0, \tag{2.1b}$$

$$\frac{\partial c^{\pm *}}{\partial t^*}+\boldsymbol{v}^*\cdot\boldsymbol{\nabla}^* c^{\pm *}=D^*\boldsymbol{\nabla}^*\cdot\left(\boldsymbol{\nabla}^* c^{\pm *}\pm V_{\mathrm{T}}^{*-1}c^{\pm *}\boldsymbol{\nabla}^*\phi^*\right), \tag{2.1c}$$

$$-\varepsilon^*\nabla^{*2}\phi^*=\rho_e^*, \tag{2.1d}$$

in which $\boldsymbol{v}^*$, $p^*$, $c^{+*}$, $c^{-*}$, and $\phi^*$ are the fluid velocity, hydrodynamic pressure, cation concentration, anion concentration, and electrostatic potential, respectively. Moreover, $\boldsymbol{E}^*=-\boldsymbol{\nabla}^*\phi^*$ is the electric field, $\rho_e^*=ze^*(c^{+*}-c^{-*})$ is the free charge density, and $\rho^*$, $\mu^*$, $D^*$, $V_{\mathrm{T}}^*=k_{\mathrm{B}}^*T^*/(ze^*)$, $\varepsilon^*$, and $z$ are the fluid mass density, fluid viscosity, ionic diffusivity, thermal voltage, dielectric permittivity, and ionic valence, respectively. Finally, $e^*$, $k_{\mathrm{B}}^*$ and $T^*$ are the elementary charge, Boltzmann constant, and temperature, respectively.

### 2.1. *Dimensionless formulation*

We scale time by the diffusion time $t_{\mathrm{diff}}^*=L^{*2}/D^*$, spatial coordinates by the surface-to-reservoir distance $L^*$, velocity by the diffusion velocity $v_{\mathrm{diff}}^*=D^*/L^*$, concentration by the reservoir concentration $c_{\mathrm{res}}^*$, pressure by the osmotic pressure $p_0^*=\mu^*D^*/L^{*2}$, electric potential by the thermal voltage $V_{\mathrm{T}}^*=k_{\mathrm{B}}^*T^*/(ze^*)$, and ionic flux by the diffusion flux $j_0^*=D^*c_{\mathrm{res}}^*/L^*$. The governing equations in dimensionless form become:

$$\frac{1}{Sc}\left[\frac{\partial \boldsymbol{v}}{\partial t}+\left(\boldsymbol{v}\cdot\boldsymbol{\nabla}\right)\boldsymbol{v}\right]=-\boldsymbol{\nabla}p+\nabla^2\boldsymbol{v}+\kappa\nabla^2\phi\boldsymbol{\nabla}\phi, \tag{2.2a}$$

$$\boldsymbol{\nabla}\cdot\boldsymbol{v}=0, \tag{2.2b}$$

$$\frac{\partial c^{\pm}}{\partial t}+\boldsymbol{v}\cdot\boldsymbol{\nabla}c^{\pm}=\boldsymbol{\nabla}\cdot\left(\boldsymbol{\nabla}c^{\pm}\pm c^{\pm}\boldsymbol{\nabla}\phi\right), \tag{2.2c}$$

$$-2\epsilon^2\nabla^2\phi=c^+-c^-. \tag{2.2d}$$

Here, the anion $\boldsymbol{j}^-$ and cation $\boldsymbol{j}^+$ fluxes are given as:

$$\boldsymbol{j}^{\pm}=c^{\pm}\boldsymbol{v}-\boldsymbol{\nabla}c^{\pm}\mp c^{\pm}\boldsymbol{\nabla}\phi, \tag{2.3}$$

which include advective, diffusive, and electromigration terms.

In our studies, the two most significant dimensionless groups governing the problem are the dimensionless applied voltage $\Delta V$ and the dimensionless screening length $\epsilon$,

$$\Delta V = \frac{\Delta V^*}{V_{\mathrm{T}}^*}, \quad \epsilon = \frac{\lambda_{\mathrm{D}}^*}{L^*}, \tag{2.4}$$

where $\lambda_{\mathrm{D}}^* = \sqrt{\varepsilon^* k_{\mathrm{B}}^* T^* / [2(ze^*)^2 c_{\mathrm{res}}^*]}$ is the Debye–Huckel screening length. The remaining dimensionless groups are the electrohydrodynamic coupling constant $\kappa = \varepsilon^* V_{\mathrm{T}}^{*2} / \mu^* D^*$, the Schmidt number $Sc = \mu^*/(\rho^* D^*)$, and the fixed concentration $\beta$ of the counterions on the charge-selective surface.

## 3. 2D DNS of electro-osmotic chaos at flat membrane

### 3.1. *Model problem*

As shown in Figure 1a, we consider a symmetric binary electrolyte between an ion-selective surface and a stationary reservoir subject to an applied voltage $\Delta V^*$. The top boundary sustains a fixed salt concentration $c_{\mathrm{res}}^*$ controlled by the stationary reservoir, and the bottom boundary is impermeable to anions and freely permeable to cations. In this particular study we neglect inertial effects on the flow, i.e., $(1/Sc)\mathrm{d}\boldsymbol{v}/\mathrm{d}t = 0$.

### 3.2. *Boundary conditions*

On the ion-selective surface at $y = 0$, there is no-slip $\boldsymbol{v} = \boldsymbol{0}$, a grounded potential $\phi = 0$, a fixed cation concentration $c^+ = \beta$, and no-flux condition $j_n^- = 0$ for anions, while on the reservoir boundary at $y = 1$, there is no-slip $\boldsymbol{v} = \boldsymbol{0}$, an applied potential $\phi = \Delta V$, and fixed cation and anion concentration $c^+ = c^- = 1$. We employ periodic boundary conditions in the transverse direction, and we select an initial condition by applying a small perturbation on the 1D steady solution.

The values of the dimensionless groups considered in this study are $\epsilon = 10^{-3}$, $\Delta V = 20$ to 120, $\kappa = 0.5$, and $\beta = 2$. We report computational details elsewhere (Druzgalski *et al.* 2013).

### 3.3. *Results*

#### 3.3.1. *Chaotic snapshot*

Before we proceed with a more quantitative analysis of the chaotic transport, we show in Figure 2 a snapshot of the salt concentration $(c^+ + c^-)/2$ for an applied voltage $\Delta V = 120$. The snapshot underlines in a compelling way one of the main findings of the present work: namely, that the system is far from being quasi-steady, but instead is chaotic with features that exhibit large separation in both time and length scales.

#### 3.3.2. *Current fluctuations and overlimiting current*

The current density $\boldsymbol{i}$ is driven by advection, diffusion, and conduction,

$$\boldsymbol{i} = \boldsymbol{j}^+ - \boldsymbol{j}^- = \rho_e \boldsymbol{v} - \boldsymbol{\nabla}\rho_e - c\boldsymbol{\nabla}\phi, \tag{3.1}$$

where $\rho_e = c_+ - c_-$ is the dimensionless charge density. The (positively signed) $x$-averaged normal-component of the current density on the reservoir boundary is

$$I = -\frac{1}{a}\int_0^a i_y(x, y = 1, t)\mathrm{d}x, \tag{3.2}$$

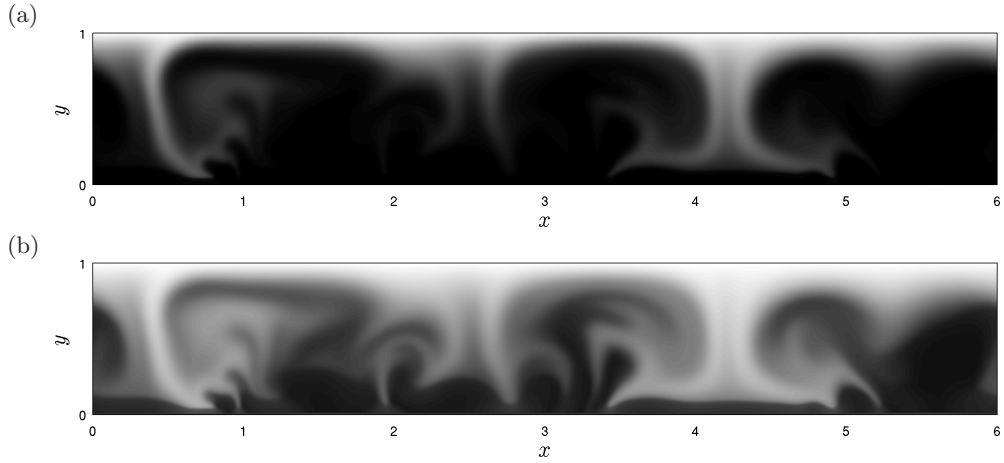


FIGURE 2. Snapshots of the salt concentration $c = (c^+ + c^-)/2$ through different mappings: (a) linear, $c$, and (b) nonlinear, $c^{1/3}$. For an applied voltage $\Delta V = 120$ and a screening length $\epsilon = 10^{-3}$. White and black colors correspond to high and low values, respectively.

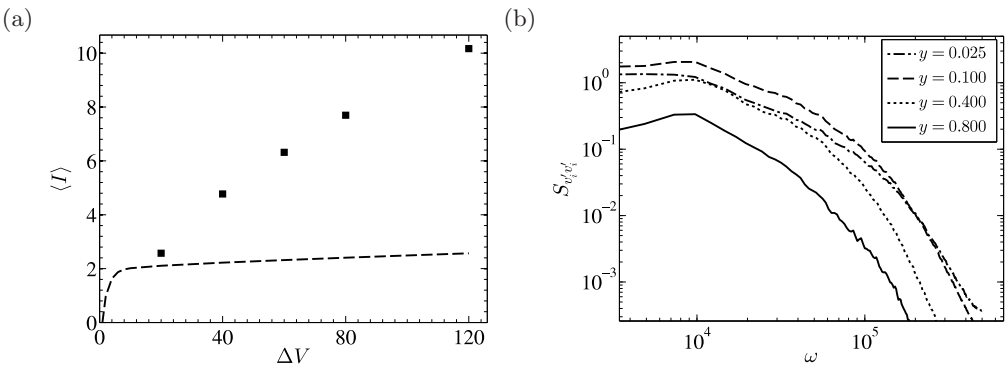


FIGURE 3. (a) Time- and $x$-averaged current density $\langle I \rangle$ versus applied voltage $\Delta V$ in the case of the original 2D formulation with flow (square symbols) and in a case without flow leading to 1D transport (dashed curve). (b) Log-log plot of the energy spectral density $S_{v_i'v_i'}$ at different wall-normal distances versus angular frequency $\omega$ for $\Delta V = 120$. Here, approximately 7000 time data samples are used.

where $a$ is the dimensionless width of the domain. After the current has entered the statistically stationary state, we calculate the time- and $x$-averaged current density $\langle I \rangle$,

$$\langle I \rangle = \frac{1}{\tau} \int_{t_0}^{t_0+\tau} I \, \mathrm{d}t. \tag{3.3}$$

Throughout this section, the onset of statistical steady state is $t_0 = 0.1$ and the time span is $\tau = 0.8$ (corresponding to 7000 data samples in time). Figure 3a shows $\langle I \rangle$ versus $\Delta V$ for two models: (i) with chaos from the 2D calculation and (ii) without chaos from a 1D model. It is clear that the 2D model predicts OLC that is qualitatively in much better agreement with experimental observations when compared to the quiescent 1D model (Maletzki *et al.* 1992; Rubinstein *et al.* 2008; Kwak *et al.* 2013). Based on the five 2D data points, the current in the OLC regime varies approximately linearly with the applied voltage.

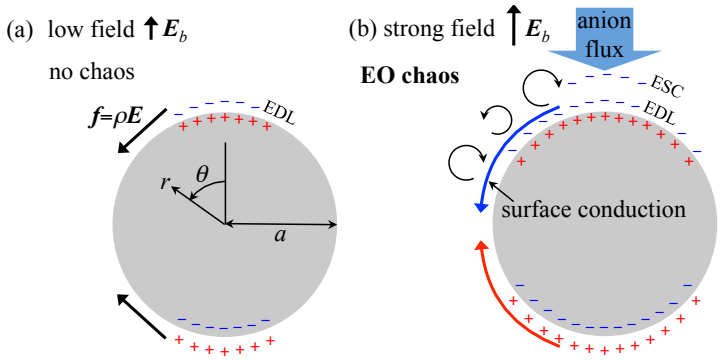


FIGURE 4. Schematic of key elements of ICEO in a binary electrolyte around an ideally polarizable cylinder subject to an external electric field $E_b^*$. (a) Low field. (b) High field.

3.3.3. *Broadband energy spectrum*

We introduce the decomposition of a quantity $f$ into an average $\overline{f}$ and a fluctuation $f'$, i.e., $f(x,y,t) = \overline{f}(y) + f'(x,y,t)$,

$$\overline{f}(y) = \frac{1}{a\tau}\int_{t_0}^{t_0+\tau}\int_0^a f(x,y,t)\,\mathrm{d}x\mathrm{d}t, \tag{3.4}$$

where $t_0$ is a time after the statistically stationary chaos is fully developed. The decomposition is strictly defined in the limit $\tau \to \infty$, but we use finite $\tau$ that is sufficiently large to ensure statistical convergence.

Figure 3b shows the energy spectral density $S_{v_i'v_i'} = S_{u'u'} + S_{v'v'}$ versus frequency $\omega$ at wall-normal distances $y = 0.025$, 0.1, 0.4, and 0.8 for $\Delta V = 120$. The energy spectral density is the distribution of the kinetic energy in the flow over a range of temporal frequencies. The broadband structure of $S_{v_i'v_i'}$ confirms that the flow is chaotic. Any periodic flow component would result in distinct peaks in $S_{v_i'v_i'}$.

## 4. 2D DNS of electro-osmotic chaos at cylindrical polarizable object

### 4.1. *Introduction*

As shown in Figure 4, in this section, we extend our studies to Induced-Charge Electro-Osmosis (ICEO) which refers to flows driven by electrostatic forces arising from the action of an applied electric field on free charge induced by the field itself in nanometer-thin boundary layers on the surface of a polarizable object (Bazant 2011). Within the past decade, ICEO has received considerable attention as a means for mixing and pumping in microfluidic lab-on-a-chip systems, which are typically used for biochemical analysis.

In the late 1990s, Ramos and coworkers discovered AC electroosmosis (Ramos *et al.* 1998), a particular variant of ICEO, and some years later, a more general theoretical description of ICEO was developed by Bazant and Squires (Bazant & Squires 2004; Squires & Bazant 2004). Figure 4 presents a canonical ICEO problem showing an ideally polarizable cylinder fixed in a binary aqueous electrolyte. An external electric field $E_b^*$ drives ions in the bulk and induces a local electric double layer (EDL) on the surface of the cylinder. After full charging of the EDL, the surface will act as an insulator to the external current. Ignoring surface conduction and assuming uniform bulk conductivity, Bazant and Squires solved the Laplace equation subject to Neumann boundary conditions for low fields. They computed the tangential electric field outside of the EDL to be

$E^*_\theta = -2E^*_b \sin(\theta)$ where $\theta$ is the angle relative to the direction of the electric field. Given the uniform potential of the cylinder, the induced zeta potential across the thin EDL was computed to be $\zeta^* = 2E^*_b a^* \cos(\theta)$ in which $a^*$ is the cylinder radius. Using the Helmholtz–Smoluchowski relation (Probstein 1994), they predicted that the tangential field acting on the EDL should lead to an induced slip velocity with quadratic dependence on the electric field, $U^* \sim E^{*2}_b$. The quadratic dependence of the induced flow in ICEO offered promising advantages over linear electroosmotic flow systems: namely, flow-rates faster than linear electroosmosis at high voltages and a net flow even under AC forcing, thus *avoiding* electrode reactions or bubble formation.

However, after recent comparisons with experimental measurements, it became clear that ICEO velocities in practice are lower than those predicted by the *low-field asymptotic model* of Bazant and Squires (Bazant & Squires 2004). Particularly at high voltages, the discrepancy can be up to an order of magnitude (Bazant *et al.* 2009).

To explain this discrepancy, several modifications have been proposed. The majority of the papers in the literature have attributed the differences to non-continuum effects and have attempted to provide better fits to the experimental data by invoking models taking into account corrections such as Stern layer and ion packing near the surface (Bazant *et al.* 2009). Most recently, studies have been conducted to take into account effects of surface conduction (Gregersen *et al.* 2009) and bulk concentration polarization (Schnitzer & Yariv 2012). However, all of the models considered so far are based on asymptotic simplifications assuming a quasi-electroneutral bulk adjacent to a thin EDL. Additionally, previous models assume that flow and transport in ICEO systems are stable and steady.

We have recently performed DNS of the coupled Poisson–Nernst–Plank and Navier–Stokes equations for a configuration shown in Figure 4 and confirmed that ICEO at high voltage is indeed unstable, even chaotic. While we defer discussions on the cause of such instabilities to a future publication, we here briefly point out that strong ion-selective surface conduction leads to the formation of local ESC layers and the development of an instability very similar to that at a flat membrane.

The equations Eq. (2.1a-d) are solved in 2D around a metallic cylinder. The boundary conditions on the cylinder ($r^* = a^*$) are no-flux, no-slip, and fixed potential. In the far field, we enforce fixed concentration $c^{+*} = c^{-*} = c^*_0$, zero flow, and uniform electric field $E^*_b$. The typical domain size is taken to be $\approx 100a^*$, which is sufficiently large to ensure independence of the results on the boundary location.

The dimensionless parameters of the problem are the electrohydrodynamic coupling constant $\kappa = \varepsilon^* V^{*2}_{\mathrm{T}}/(\mu^* D^*)$, the Schmidt number $Sc = \mu^*/(\rho^* D^*)$, the dimensionless applied field $E^*_b a^*/V^*_{\mathrm{T}}$, and the dimensionless Debye length $\epsilon = \lambda^*_{\mathrm{D}}/a^*$. Note that the reference length scale in this problem is the radius of the cylinder $a^*$.

In this brief, we consider $\kappa = 0.5$ and $Sc = 10^3$ consistent with typical aqueous electrolytes. The applied field is varied from below thermal voltage up to $E^*_b a^*/V^*_{\mathrm{T}} = 50$. $\epsilon$ is taken to be equal to $\epsilon = 10^{-3}$ (e.g., representing a 20-$\mu$m-diameter cylinder in a 1-mM electrolyte). The computational details are reported elsewhere.

### 4.2. *Results*

Our DNS calculations indicate that instability and chaos can develop in ICEO with a significant impact on the system-level response. Furthermore, these results are unlikely to have been discovered using purely asymptotic methods as has been the tradition in the field of electrokinetics.

Figure 5 shows a snapshot for $E^*_b a/V_{\mathrm{T}} = 50$ of the dimensionless salt concentration

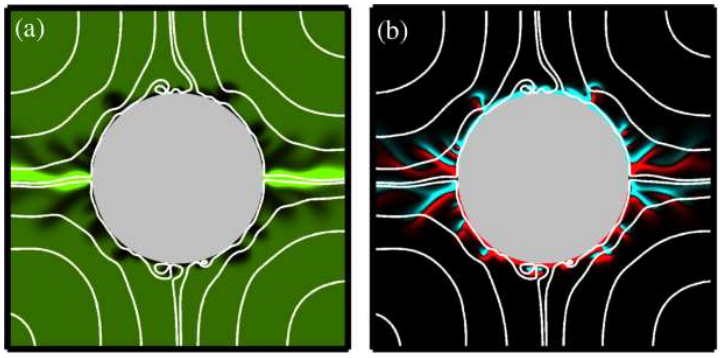


FIGURE 5. Instantaneous snapshot of: (a) dimensionless salt concentration (green=high, black=low) and (b) dimensionless free charge density (red=positive, blue=negative). Streamlines are superimposed. Parameters are $\epsilon = 10^{-3}$ and $E_b^* a^*/V_T^* = 50$.

$(c^{+*} + c^{-*})/(2c_0^*)$ (a) and the dimensionless free charge density $(c^{+*} - c^{-*})/c_0^*$ (b). The figures are overlayed by the instantaneous flow streamlines. The strong surface conduction is particularly evident in Figure 5(a) where it leads to the salt enrichment jets at $\theta = \pm 90°$. The instability is located at $\theta = 0°, 180°$ and leads to the formation of microvortices on top of the background ICEO flow. These microvortices in turn lead to the formation of ion-depleted void regions which are subsequently advected along the cylinder. As shown in Figure 5(b), the polarity of the induced charged on the cylinder is negative and positive on the top and bottom, respectively. Furthermore, in connection with the concentration gradients at the void regions and at the enrichment jet, local patterns of positive and negative charge are induced.

Figure 6 shows colorplots of the time-averaged concentration and flow streamlines from our DNS (a) in comparison to the low-field asymptotic model results (b). While the asymptotic model displays uniform concentration and symmetric streamlines, the DNS shows strong concentration polarization around the cylinder (even after time averaging), with ion depletion starting at $\theta = 0°, 180°$ and advecting towards $\theta = \pm 90°$. Furthermore, a strong salt enrichment jet due to ejection of ions via the surface-conduction mechanism is observed.

The difference in the streamlines in Figure 6a and b indicates the difference between the flow fields, with the spacing between streamlines being inversely proportional to velocity. The time-averaged flow from the DNS is much smaller than that from the low-field asymptotic model by a factor up to $\approx 5$.

## 5. 2D spatio-temporal linear stability of electro-osmosis in cross-flow at flat membrane

### 5.1. *Introduction*

As shown in Figure 1b, in this section we present our third and last case in this brief: a spatio-temporal stability analysis of EOI in a cross-flow. This is motivated both by the recent experimental observations by Kwak *et al.* (2013) and by the fact that in many applications a cross-flow is needed to supply and extract the electrolyte. Our spatio-temporal investigation therefore extends previous purely temporal stability studies. Furthermore, we verify the methodology by comparison to a 2D linear impulse response calculation of

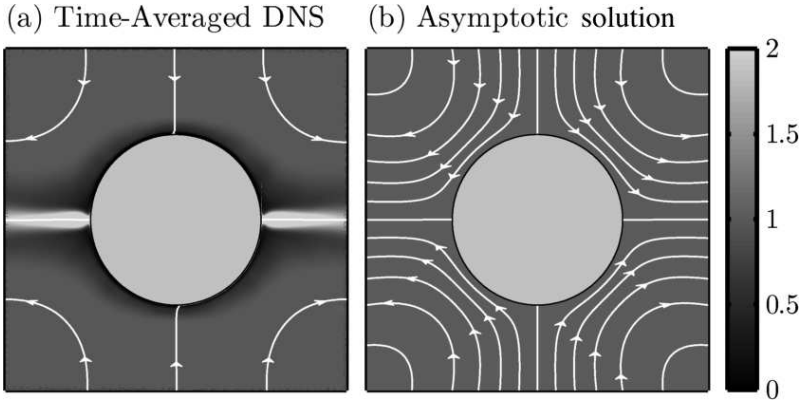


FIGURE 6. Gray-scale plots of the time-averaged salt concentration and flow streamlines for $E_b^* a^*/V_T^* = 50$, highlighting the difference in ICEO calculations by (a) the DNS and (b) the low-field asymptotic model.

a validated DNS code (Druzgalski *et al.* 2013). For reference, Figure 1 shows a schematic of EOI both with and without cross-flow.

### 5.2. *Flow configuration*

As shown in Figure 1(b), we consider a binary electrolyte flowing in the $x^*$-direction between two parallel plates of separation $h^*$. At the bottom plate boundary, the inert non-charged material is replaced with a charge-selective media at $x^* = 0$. Upstream, we assume a fully developed plane-Poiseuille flow. To understand the fundamentals of the problem, we idealize the system by modeling the top anion-selective plate as a stationary reservoir of fixed concentration and the bottom plate as an ideal cation-selective surface.

For $x^* > 0$, the top and bottom plates are maintained at uniform electric potentials with a relative difference of $\Delta V^*$. The voltage difference drives an electric current between the plates, and both cations and anions deplete at the bottom cation-selective surface. The ion depletion layer grows downstream and its structure consists of the EDL, the ESC, and the DL, as shown in Figure 1(b). We assume that ion transport by streamwise advection relative to wall-normal electro-diffusion, embodied by the Péclet number $Pe = u^*_{\max} h^*/D^*$, is large such that the depletion layer for sufficiently large $x^*$ grows slowly with downstream position and therefore is locally parallel to the plates.

We note that the non-dimensionalization in this section is slightly different from that of the previous cases. The governing dimensionless groups remain the same, but the scales of time, velocity and pressure are changed. In particular, we scale velocity by the electroviscous velocity $u^*_{\rm ev} = \varepsilon^* V_T^{*2}/(\mu^* h^*)$, time by the electroviscous advection time $t^*_{\rm ev} = h^*/u^*_{\rm ev}$, and pressure by the electroviscous pressure $p^*_{\rm ev} = \mu^* u^*_{\rm ev}/h^*$.

#### 5.2.1. *Boundary conditions*

We continue in the dimensionless notation. At the bottom cation-selective wall we assume a no-slip condition for the fluid and a grounded electrostatic potential. We follow the literature (Zaltzman & Rubinstein 2007) and model the ideal selectivity by a fixed cation concentration $\beta$ and a zero anion mass flux,

$$u = 0, \quad v = 0, \quad \phi = 0, \quad c^+ = \beta, \quad -\frac{\partial c^-}{\partial y} + c^- \frac{\partial \phi}{\partial y} = 0, \qquad \text{at } y = 0. \tag{5.1}$$

At the top wall, which we idealize as a reservoir, we assume no-slip of the hydrodynamic flow, a biased electrostatic potential and fixed cation and anion concentrations,

$$u = 0, \qquad v = 0, \qquad \phi = \Delta V, \qquad c^+ = 1, \qquad c^- = 1, \qquad \text{at } y = 1. \tag{5.2}$$

We remind the readers that the dimensionless groups were defined in Section 2.1 and we use the fixed values $\kappa = 0.5$, $Sc = 10^3$ and $\beta = 2$, whereas we will vary $\Delta V$, $Pe$ and $\epsilon$.

### 5.3. *Regular perturbation expansion*

Having formulated the model problem, we proceed by considering the stability of the initially steady base cross-flow to infinitesimal perturbations. To this end, we assume the problem can be treated as locally parallel, and for fixed downstream position we expand all the variables in a regular perturbation expansion. The perturbation is decomposed into Fourier modes in both time and downstream coordinate,

$$u(x, y, t) = u_0(x, y) + u_1(x, y, t), \tag{5.3a}$$

$$u_1(x, y, t) = \mathrm{Re}\left[\int_{-\infty}^{\infty}\int_{-\infty}^{\infty} \hat{u}_1(\alpha, y, \omega)\, e^{i(\alpha x - \omega t)}\, \mathrm{d}\alpha\, \mathrm{d}\omega\right], \tag{5.3b}$$

where subindex 0 and 1 indicates a base state and perturbation state, respectively, a hat indicates a complex Fourier mode amplitude, $\alpha$ is the complex wavenumber, and $\omega$ is the complex frequency. Substitution of Equations (5.3) into the governing equations and boundary conditions with subsequent matching of terms of equal order leads to governing equations for the base state, denoted with subindex 0, and to a generalized eigenvalue problem for the perturbations, denoted with subindex 1.

#### 5.3.1. *Base state*

The base-state hydrodynamic flow is zero in the wall-normal direction and given by the imposed Poiseuille-flow parabolic velocity profile in the streamwise direction, $u_0 = Pe\, 4y\,(1-y)/\kappa$, where $Pe = u^*_{\max} h^*/D^* = \kappa u^*_{\max}/u^*_{\mathrm{ev}}$. Due to the slow variation of the variables in the downstream direction, the base-state governing equations for the electrostatic potential reduce to a purely one-dimensional Poisson equation. For the ion mass conservation, the equations reduce to a balance between wall-normal electro-diffusion and streamwise advection when we assume strong streamwise advection, $\kappa \max(u_0) = Pe \gg 1$.

We do a scaling analysis by balancing wall-normal diffusion and streamwise advection to obtain an estimate of the depletion layer width $\delta = [x/(4Pe)]^{1/3}$. The downstream position at which the problem becomes locally parallel can be estimated from the requirement $\partial_x \delta \ll 1$ which leads to the condition $x \gg 0.1\,(Pe)^{-1/2}$ (partial and total derivatives denoted by $\partial_x$ and $\mathrm{d}_x$, respectively). We introduce the self-similarity variable $\eta = y/\delta = y[x/(4Pe)]^{-1/3}$ whereby $\partial_y = \mathrm{d}_\eta/\delta$ and $\partial_x = -\eta \mathrm{d}_\eta/(3x)$ (Probstein 1994). The base state PDEs reduce to ODEs,

$$-2\left(\frac{\epsilon}{\delta}\right)^2 \frac{\mathrm{d}^2\phi_0}{\mathrm{d}^2\eta} = c_0^+ - c_0^-, \tag{5.4a}$$

$$-\frac{\eta^2}{3}\,(1-\delta\eta)\,\frac{\mathrm{d}c_0^\pm}{\mathrm{d}\eta} = \frac{\mathrm{d}}{\mathrm{d}\eta}\left(\frac{\mathrm{d}c_0^\pm}{\mathrm{d}\eta} \pm c_0^\pm \frac{\mathrm{d}\phi_0}{\mathrm{d}\eta}\right). \tag{5.4b}$$

A true similarity problem will be achieved for both $\delta \ll 1$ and $\epsilon/\delta \ll 1$, where Eq. (5.4) reduces to an ODE independent of $\delta$. However, $\epsilon/\delta \ll 1$ is a singular limit, and a mathematically rigorous solution would employ methods of matched asymptotic expansions

resulting in a similarity solution for the outer electroneutral diffusion layer. Additionally, there exists an inner region consisting of the ESC and EDL layers, with quasi-steady response in $x$, which is matched to the outer diffusion layer. By keeping the $\delta$-dependent term in Eq. (5.4*a*) and solving the problem numerically for each $x$, we bypass the need for an asymptotic method. In the same manner, we keep the other $\delta$-dependent terms to obtain a better approximation to the original PDEs. This procedure results in a base state that captures the main features of an exact solution.

5.3.2. *First-order fields; perturbation*

Having determined the base state, we proceed by developing the eigenvalue problem governing the perturbation. Using the perturbation expansion Eq. (5.3*a*) in the governing equations and equating terms of first order, we obtain a system of linear, second-order PDEs. Then, using the Fourier expansion Eq. (5.3*b*), these equations reduce to ODEs in the wall-normal direction which can be written as a generalized eigenvalue problem,

$$\mathsf{A}\,\hat{\boldsymbol{q}}_1 = \mathrm{i}\lambda \mathsf{B}\,\hat{\boldsymbol{q}}_1, \tag{5.5}$$

where the eigenvalue $\lambda$ and the eigenfunction vector $\hat{\boldsymbol{q}}_1$ have two different definitions depending on the analysis: (1) for temporal analysis, $\lambda = \omega$ and $\hat{\boldsymbol{q}}_1 = [\hat{u}_1\, \hat{v}_1\, \hat{p}_1\, \hat{\phi}_1\, \hat{c}_1^+\, \hat{c}_1^-]^\top$ and (2) for spatial analysis, $\lambda = \alpha$ and $\hat{\boldsymbol{q}}_1 = [\hat{u}_1\, \hat{v}_1\, \hat{v}_{1x}\, \hat{p}_1\, \hat{\phi}_1\, \hat{\phi}_{1x}\, \hat{c}_1^+\, \hat{c}_{1x}^+\, \hat{c}_1^-\, \hat{c}_{1x}^-]^\top$.

We can characterize the spatio-temporal stability into three classes: (i) stable, (ii) convectively unstable, and (iii) absolutely unstable. The significance of these three stability categories is as follows. Stability is when a local perturbation decays everywhere. Convective instability is when a local perturbation only grows downstream of its point of introduction. Absolute instability is when a local perturbation grows both downstream and upstream to its point of introduction. In other words, in the long-time limit, only in the case of absolute instability will the perturbation be sustained; the perturbation eventually leaves the system for both stability and convective instability conditions. To determine which stability category a given configuration of our system falls into, we perform both a temporal and a spatial analysis. From the temporal stability analysis we determine the temporal growth rate $\omega_{i,\max}$ and from the spatial analysis we determine the absolute growth rate $\omega_{i,0}$, where it always holds that the temporal growth rate is greater than or equal to the absolute growth rate $\omega_{i,\max} \geq \omega_{i,0}$. Without giving further details, the system is stable if $\omega_{i,\max} < 0$ and $\omega_{i,0} < 0$, convectively unstable if $\omega_{i,\max} > 0$ and $\omega_{0,i} < 0$, and absolutely unstable if $\omega_{i,\max} > 0$ and $\omega_{0,i} > 0$.

## 5.4. *Results*

We have solved the stability problem above and obtained both $\omega_{0,i}$ and $\omega_{i,\max}$ at many downstream positions, in the range of $0.01 < x < 50$, for all combinations of the control parameters $\epsilon = [10^{-4}, 10^{-3}, 10^{-2}]$, $Pe = [10^2, 10^3, 10^4]$, and $\Delta V = [20, 30, 40, 60]$.

5.4.1. *Absolute and convective growth rates versus downstream position*

We present in Figure 7 the growth rates as a function of downstream position in a voltage-Péclet matrix. In some cases the instability occurs only in a finite window of downstream positions, whereas in other cases the growth rate levels off towards a non-zero plateau for large $x$.

Figure 7 shows that the convective growth rate $\omega_{i,\max}$ is always larger than the absolute growth rate $\omega_{0,i}$ as expected, but the two have a negligible difference in large parts of the absolutely unstable regime. This implies that the absolute mode coincides with the

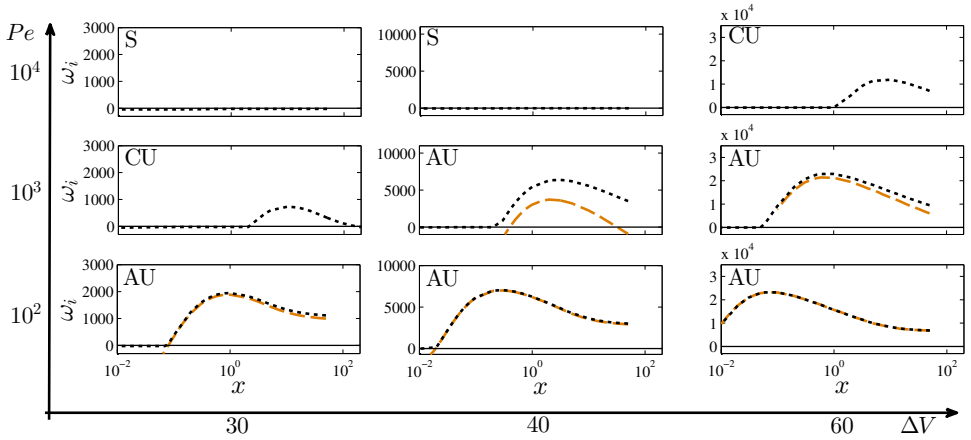


FIGURE 7. Matrix of subplots with each subplot corresponding to a different voltage $\Delta V$ and Péclet number $Pe$ as indicated by the major axis for $\epsilon = 10^{-3}$. Individual subplots show absolute $\omega_{0,i}$ (dashed, orange line) and maximum $\omega_{i,\max}$ (dotted, black line) growth rate versus downstream position.

peak of the wavepacket, and suggests that the cross-flow has a direct diminishing effect upon the instability, well inside the absolutely unstable regime. Taking into account the plots for $\epsilon = 10^{-4}$ and $10^{-2}$ (data shown elsewhere), $\omega_{i,\max}$ and $\omega_{0,i}$ are approximately equal in the regime of absolute instability except close to the transition to convective instability.

Cross-flow has an indirect effect, however, by influencing the development of the base flow. Figure 7 shows that for fixed voltage, the cross-flow displaces the growth-rate curves downstream, also determining the stability of the system. For example, for $\Delta V = 60$, going from $Pe = 10^2$ to $10^3$ moves the maximum from $x \approx 10^{-1}$ to $10^0$, but its value remains at around $2 \times 10^4$.

### 5.4.2. *Stability phase map*

Figure 8 characterizes the overall stability of the system in the voltage-Péclet plane for different screening lengths $\epsilon$. The stability criterion is established by considering the maximum of the growth rate over all downstream positions, i.e., stable if $\max_x(\omega_{0,i}) < 0$ and $\max_x(\omega_{i,\max}) < 0$, convectively unstable if $\max_x(\omega_{0,i}) < 0$ and $\max_x(\omega_{i,\max}) > 0$, and absolutely unstable if $\max_x(\omega_{0,i}) > 0$. Below a critical voltage $\Delta V_* \approx 21$, the system is unconditionally stable.

In general, increasing the voltage takes the system from stable, through convectively unstable, to absolutely unstable, and increasing the Péclet number has the reverse effect. However, it is clear that the system is more stable for larger screening lengths and that the window of convective instability shrinks with decreasing screening length. At the same time, with decreasing screening length, the threshold for convective and absolute instability moves towards smaller voltages and higher Péclet numbers.

## 6. Summary

We have shown the feasibility and utility of DNS tools for computation and analysis of nonlinear electrokinetic flows. Specifically, we have used the DNS tools to show that chaotic transport similar to turbulence arises in electrokinetic systems near ion-selective

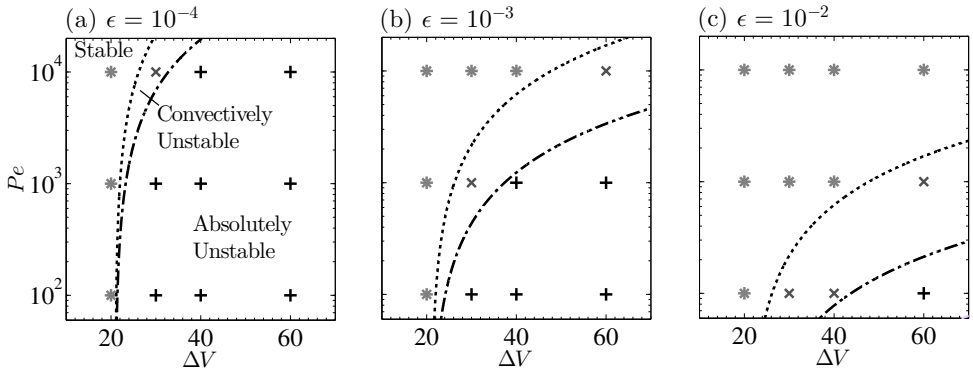


FIGURE 8. Stability characterization in the voltage-Péclet plane with indication of where the system is stable (star symbol), convectively unstable (cross symbol), and absolutely unstable (plus symbol) for (a) $\epsilon = 10^{-4}$, (b) $\epsilon = 10^{-3}$ and (c) $\epsilon = 10^{-2}$.

surfaces at high forcing and even at low Reynolds numbers. The challenges in carrying out these high-fidelity DNS computations are similar to those for turbulent boundary layers, such as parallel computing and resource management, albeit with the added complexity of additional physics and stricter requirements for the time integration.

In addition to our DNS results, we have also performed a linear stability analysis of electro-osmotic instability subject to a cross-flow. This work extends previous analyses which have not considered background shear. We have mapped the entire parameter space into stable, convectively unstable, and absolutely unstable regimes, thereby showing the effects of the strength of the cross-flow, applied voltage, and Debye screening length. Our main finding is that background shear has a stabilizing effect on electro-osmotic instability.

## Acknowledgments

The authors gratefully acknowledge helpful comments from Dr. Elif Karatay that significantly improved the quality of this brief. The authors also acknowledge computing and visualization time on the Certainty cluster at Stanford (MRI-R2 NSF Award 0960306).

## REFERENCES

ANDERSEN, M. B., SOESTBERGEN, M. V., MANI, A., BRUUS, H., BIESHEUVEL, P. M. & BAZANT, M. Z. 2012 Current-induced membrane discharge. *Phys. Rev. Lett.* **109** (10), 108301.

BAZANT, M. Z. 2011 Induced-charge electrokinetic phenomena. In *Electrokinetics and Electrohydrodynamics in Microsystems* (ed. A. Ramos), *CISM Courses and Lectures* 530, pp. 221–297. Springer, Vienna.

BAZANT, M. Z., KILIC, M. S., STOREY, B. D. & AJDARI, A. 2009 Towards an understanding of induced-charge electrokinetics at large applied voltages in concentrated solutions. *Adv. Colloid Interface Sci.* **152** (1-2), 48–88.

BAZANT, M. Z. & SQUIRES, T. M. 2004 Induced-charge electrokinetic phenomena: Theory and microfluidic applications. *Phys. Rev. Lett.* **92** (6), 066101.

CHANG, H.-C., YOSSIFON, G. & DEMEKHIN, E. A. 2012 Nanoscale electrokinetics and

microvortices: How microhydrodynamics affects nanofluidic ion flux. *Annu. Rev. Fluid Mech.* **44** (1), 401–426.

Druzgalski, C. L., Andersen, M. B. & Mani, A. 2013 Direct numerical simulation of electroconvective instability and hydrodynamic chaos near an ion-selective surface. *Phys. Fluids* **25** (11), 110804.

Gregersen, M. M., Andersen, M. B., Soni, G., Meinhart, C. & Bruus, H. 2009 Numerical analysis of finite Debye-length effects in induced-charge electro-osmosis. *Phys. Rev. E* **79** (6), 066316.

Kwak, R., Guan, G., Peng, W. K. & Han, J. 2013 Microscale electrodialysis: Concentration profiling and vortex visualization. *Desalination* **308**, 138–146.

Levich, V. & Spalding, D. 1962 *Physicochemical hydrodynamics*, , vol. 689. Prentice-Hall Englewood Cliffs, NJ.

Maletzki, F., Rösler, H.-W. & Staude, E. 1992 Ion transfer across electrodialysis membranes in the overlimiting current range: stationary voltage current characteristics and current noise power spectra under different conditions of free convection. *J. Membr. Sci.* **71** (1-2), 105–116.

Newman, J. & Thomas-Alyea, K. 2004 *Electrochemical systems*. Wiley-Interscience.

Nikonenko, V. V., Pismenskaya, N. D., Belova, E. I., Sistat, P., Huguet, P., Pourcelly, G. & Larchet, C. 2010 Intensive current transfer in membrane systems: Modelling, mechanisms and application in electrodialysis. *Adv. Colloid Interface Sci.* **160** (1-2), 101–123.

Pourcelly, G., Nikonenko, V. V., Pismenskaya, N. D. & Yaroslavtsev, A. B. 2012 Applications of charged membranes in separation, fuel cells, and emerging processes. In *Ionic Interactions in Natural and Synthetic Macromolecules* (ed. A. Ciferri & A. Perico), pp. 761–815. John Wiley & Sons, Inc.

Probstein, R. 1994 *Physicochemical Hydrodynamics: An Introduction*. John Wiley & Sons.

Ramos, A., Morgan, H., Green, N. G. & Castellanos, A. 1998 Ac electrokinetics: a review of forces in microelectrode structures. *J. Phys. D: Appl. Phys.* **31** (18), 2338.

Rubinstein, I. & Zaltzman, B. 2000 Electro-osmotically induced convection at a permselective membrane. *Phys. Rev. E.* **62** (2), 2238.

Rubinstein, S. M., Manukyan, G., Staicu, A., Rubinstein, I., Zaltzman, B., Lammertink, R. G. H., Mugele, F. & Wessling, M. 2008 Direct observation of a nonequilibrium electro-osmotic instability. *Phys. Rev. Lett.* **101** (23), 236101.

Schnitzer, O. & Yariv, E. 2012 Induced-charge electro-osmosis beyond weak fields. *Phys. Rev. E* **86** (6), 061506.

Simons, R. 1979 Strong electric field effects on proton transfer between membrane-bound amines and water. *Nature* **280** (5725), 824–826.

Squires, T. M. & Bazant, M. Z. 2004 Induced-charge electro-osmosis. *J. Fluid Mech.* **509**, 217–252.

Strathmann, H. 2010 Electrodialysis, a mature technology with a multitude of new applications. *Desalination* **264**, 268–288.

Wang, Y.-C., Stevens, A. L. & Han, J. 2005 Million-fold preconcentration of proteins and peptides by nanofluidic filter. *Anal. Chem.* **77** (14), 4293–4299.

Weber, A. Z., Mench, M. M., Meyers, J. P., Ross, P. N., Gostick, J. T. & Liu, Q. 2011 Redox flow batteries: a review. *J. Appl. Electrochem.* **41** (10), 1137–1164.

Zaltzman, B. & Rubinstein, I. 2007 Electro-osmotic slip and electroconvective instability. *J. Fluid Mech.* **579**, 173–226.

Zangle, T. A., Mani, A. & Santiago, J. G. 2010 Theory and experiments of concentration polarization and ion focusing at microchannel and nanochannel interfaces. *Chem. Soc. Rev.* **39** (3), 1014–1035.